

Quantifying Faraday Pattern and Onset Amplitude of Fluid with NMF and 2PCF Algorithms*

Xiaoyi Ouyang[†]

*School of Physics,
Peking University*

Jiaxuan Li[‡]

*Department of Astronomy,
Peking University*

(Dated: December 11, 2019)

In this paper, we first review theories on weakly nonlinear region of Faraday pattern, arriving at an approximate expression for dispersion relation and a rough explanation for hysteresis. A common predicament concerning experiments of surface wave originates from quantification of physical quantities, e.g. wavelength. We intend to apply two algorithms (i.e. NMF and 2PCF) to quantify experimental data given their unique features. In order to test the algorithms' efficacy, we further investigate the *dipole* oscillation pattern of milk under weak forcing and weak damping condition. Since dispersion relation is well-characterized in this case, we can compare dispersion relation obtained from NMF and 2PCF with theoretical one. The fitted T/ρ coincides with literature quite well. Then we focus on onset amplitude of Faraday waves and discuss on the source of unexpected hysteresis. The theoretical $\Omega-k$ relation and acceleration- Ω relation fit the experiment data well and parameters are in appropriate range.

I. INTRODUCTION

Named after Michael Faraday, classic Faraday patterns refer to nonlinear standing waves spontaneously appearing on the surface of fluid when the container is subjected to a vibrating receptacle. Patterns include stripes, squares, hexagons, and under special parameters, one can also observe other less symmetrical patterns mostly with multi-frequency forcing functions: quasi-patterns (Christiansen et al., 1992; Edwards & Fauve, 1994); superlattice patterns (SL1) (Epstein & Fineberg, 2006; Kudrolli et al., 1998); spatially subharmonic superlattice states, modulated hexagonal disorder, two mode superlattices and unlocked states (Arbell & Fineberg, 1998); oscillons (Arbell & Fineberg, 2000), and double hexagon states (Arbell & Fineberg, 1998).

Since it is impossible to explicitly write down closed-form solution of the complete Navier-Stokes equations for the Faraday problem, an alternative approach is to apply weakly nonlinear analysis within the vicinity of onset. It is known that nonlinear three-wave resonant interactions play a key role in pattern selection in Faraday wave experiments (Edwards & Fauve, 1994; Mermin & Troian, 1985; Newell & Pomeau, 1999; Porter & Silber, 2003). After applying multiple-scale analysis and simplifying with symmetry, one can arrive with a amplitude equation

having typical solutions of homogeneous(i.e. rest state), stripes, squares and hexagons. The stability of these solutions is further determined by linear stability analysis. Eventually, a final diagram of bifurcation comes in light when the unstable branches are removed. As for numerical efforts, Kumar & Tuckerman (1994) identified a numerical method to find the instability tongues that can be used for all fluid viscosities and all depths and applied it to the case of single frequency excitation. Besson et al. (1996) extended single frequency to multiple frequency excitation with Besson et al. (1996)'s method. Skeldon & Ruckridge (2015) utilized Besson et al. (1996)'s method to simulate experimental results on bifurcation sets published in: Ding & Umbanhowar (2005); Edwards & Fauve (1994); Epstein & Fineberg (2006); Kudrolli et al. (1998). The discrepancies of simulation and empirical results are within permissible range.

The paper is structured as follows. In section II, we briefly review theories on Faraday patterns and weakly nonlinear approximations. Dispersion relation and stability criterion of capillary waves are derived. In section III, we describe experiment setup and fluid samples used in this work. In section IV, we introduce Non-negative matrix factorization (NMF) and two-point correlation function (2PCF) algorithms, which allow us to do precise measurement and analysis on various Faraday patterns. In section V, we inspect the behavior of low viscosity fluid through *dipole* pattern which only appears under weak forcing and weak dissipation condition. In section VI, we investigate the behavior of viscous fluid near onset region using stability analysis. The dispersion rela-

* Both authors contributed equally to this work.

[†] ipsumo@pku.edu.cn

[‡] jiaxuan.li@pku.edu.cn

tion and acceleration relation are derived and simulated for different physical parameters. In section VII, the discrepancies between theory and experimental result are discussed.

II. BRIEF THEORY REVIEW

Infinitesimal surface waves driving parametrically evolves in the form of a damped Mathieu equation. Suppose the vibrating receptacle produces a sinusoidal motion of angular frequency Ω and amplitude \mathcal{A} , the fluid will experience apparent gravity $G(t) \equiv g - \Omega^2 \mathcal{A} \cos(\Omega t)$ in the reference moving with the container. Let $\mathbf{x} = \{x_1, x_2\}$ and y represent the horizontal and vertical Cartesian coordinates in the comoving frame. Ordinates $y = -d$, $y = 0$ and $y = \eta(\mathbf{x}, t)$ correspond to the bottom boundary, rest height level and free surface, i.e. d being the depth of fluid layer and $\eta(\mathbf{x}, t)$ representing the vertical motion.

Consider Fourier space assuming no horizontal boundary, surface waves can be dynamically described by a damped Mathieu equation (Benjamin & Ursell, 1954; Ciliberto & Gollub, 1985)

$$\frac{\partial^2 \zeta}{\partial t^2} + 2\sigma \frac{\partial \zeta}{\partial t} + \omega_0^2 [1 - F \cos(\Omega t)] \zeta = 0, \quad (1)$$

where $\zeta(\mathbf{k}, t) \equiv \iint_{-\infty}^{\infty} \eta(\mathbf{x}, t) \exp(-i\mathbf{k} \cdot \mathbf{x}) d^2 \mathbf{x}$ is the Fourier transform of horizontal motion, $\sigma = \sigma(k)$ is the viscous attenuation, $\omega_0 = \omega_0(k)$ is the angular frequency of linear waves without damping and without forcing, $F = F(k)$ is the dimensionless forcing, and \mathbf{k} being the wave vector with module $k = |\mathbf{k}|$. For capillary-gravity waves of surface tension T and density ρ

$$\omega_0^2 = (gk + \frac{T}{\rho} k^3) \tanh(kd), \quad F = \rho \Omega^2 \mathcal{A} (\rho g + Tk^2)^{-1}. \quad (2)$$

In (1), the damping coefficient σ originates from the bulk viscous dissipation and the viscous friction with the bottom in the case of shallow water. For free gravity waves in the limit of small viscosity, we have (Hough, 1896; Hunt, J. N., 1964)

$$\sigma(k) = \nu k^2 \left[2 + \frac{\coth(2kd)}{\sinh(2kd)} \right] + \sqrt{\frac{k\nu\sqrt{gd}}{8d^2}} \frac{2kd}{\sinh(2kd)}, \quad (3)$$

where ν is the fluid kinematic viscosity.

An implicit dispersion relation could be arrived from periodic solutions of (1). Such periodic solutions exhibit a series of resonance conditions for response angular frequencies ω equal to $n\Omega/2$, n being an integer (Abramowitz & Stegun, 1965). In practice, we mainly focus on $n = 1$, corresponding to *sub-harmonic* resonance. For weak forcing and damping, the exact dispersion relation can be approximately expressed in a simple form

using a standard perturbation scheme. Assuming $F \ll 1$ and $\sigma \sim O(F)$, an approximate dispersion for the sub-harmonic resonance ($\omega = \Omega/2$) is (Rajchenbach & Clamond, 2015)

$$\omega_0/\omega \approx 1 \pm \sqrt{(F/4)^2 - (\sigma/\omega^2)}, \quad (4)$$

where ω_0 is related to k via (2). The plus-minus sign here results from two separate solutions from the original equation. Note that the approximation only holds accurate near onset region.

Next weakly nonlinear approximation can be applied to the region near onset. Assuming $|kA| \ll 1$, $F \sim O(|A|^2)$ and $\sigma \sim O(|A|^2)$, amplitude equation for the slowly modulated amplitude A takes the form (Meron, 1987; Milner, 1991; Zhang & Vinals, 1997)

$$\frac{dA}{dt} + (\sigma - i\omega_0)A + \frac{iF\Omega}{8} e^{i\Omega t} A^* + \frac{iK\Omega k^2}{2} |A|^2 A = 0, \quad (5)$$

where star denotes the complex conjugate. The sign of the nonlinear term is determined by the sign of K , which in finite depth case takes the following form (Tadjbakhsh & Keller, 1960)

$$K = \frac{2 - 6s - 9s^2 - 5s^3}{16(1+s)(1-s)^2}, \quad s = \operatorname{sech}(2kd). \quad (6)$$

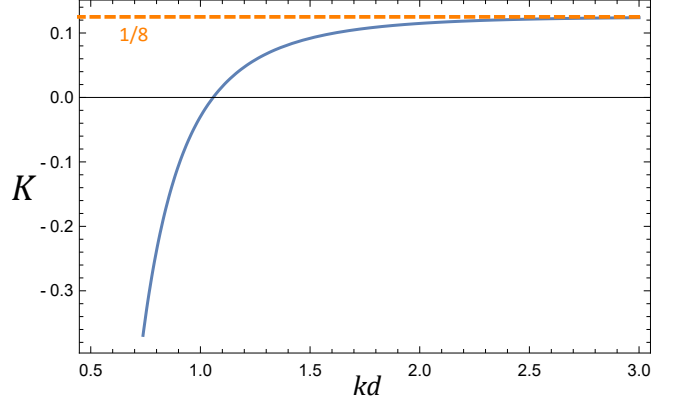


FIG. 1 $K - kd$ diagram. The definition of K can be found in (6). The nonlinear term in amplitude equation is determined by the sign of K . This diagram shows that as a function of kd , K increases monotonously and converges rapidly to $1/8$. K equals to zero when $kd \approx 1.058$.

Easily seen from Fig. 1, $K(kd)$ is a monotonously increasing function which transcends $K = 0$ when $kd \approx 1.058$. Another obvious feature is that K converges rapidly to $\lim_{kd \rightarrow \infty} K = 1/8$, which means when kd is relatively large (greater than 2), K can simply be replaced with $1/8$.

Substituting A with $B \equiv A \exp(\frac{i}{4}\pi - \frac{i}{2}\Omega t)$ in equation (5) will further simplify it into an autonomous form

(Rajchenbach & Clamond, 2015)

$$\frac{dB}{dt} = \left(i\omega_0 + \frac{\Omega}{2i} - \sigma \right) B + \frac{F\Omega}{8} B^* + \frac{K\Omega k^2}{2i} |B|^2 B, \quad (7)$$

Next we consider two typical solutions: one is the rest solution $B = 0$, the other has constant amplitude $B = a \exp(\frac{i}{4}\pi - i\delta)$, a and δ being constant. Define two thresholds of F (Rajchenbach & Clamond, 2015):

$$F_{\downarrow} = \frac{4\sigma}{\omega}, \quad (8)$$

$$F_{\uparrow} = \frac{4}{\omega} \sqrt{(\omega_0 - \omega)^2 + \sigma^2}. \quad (9)$$

Rajchenbach and Clamond had proven the following conclusions from linear stability analysis (Rajchenbach & Clamond, 2015):

1. Rest solution is stable when $F < F_{\uparrow}$ and becomes unstable when F transcends F_{\uparrow} ;
2. In constant amplitude situation, the dispersion relation has the form

$$\frac{\omega_0^{\pm}}{\omega} = 1 + K(ka)^2 \pm \sqrt{\frac{F^2}{16} - \frac{\sigma^2}{\omega^2}}, \quad (10)$$

where a is a constant that characterizes the amplitude. If $a \rightarrow 0$, the dispersion relation (4) is recovered. In general, there are also two separate solutions given the plus-minus sign. We define an upper branch ω_0^+ and a lower branch ω_0^- to denote the plus and minus dispersion relation. Note that not both branches are stable simultaneously;

3. When $K > 0$, only ω_0^- is stable after $F > F_{\uparrow}$;
4. When $K < 0$, only ω_0^+ is stable after $F > F_{\downarrow}$.

These conclusions lead directly to the bifurcation diagram, where supercritical bifurcation takes place when $K > 0$, corresponding to short waves while subcritical bifurcation happens when $K < 0$ corresponding to long waves. The region where $K < 0$ also permits hysteresis in this case.

III. EXPERIMENT SETUP

A modal shaker JZK-100 is used in this experiment to oscillate the receptacle containing target fluid. Produced by a sweep signal generator YE1311, the sinusoidal signal is magnified by a power amplifier YE5878 before the shaker receives the signal. A coil inside the modal shaker oscillates in the alternating magnetic field produced by the input signal, thus driving the plastic container fixed on the platform. The amplitude and frequency of signal

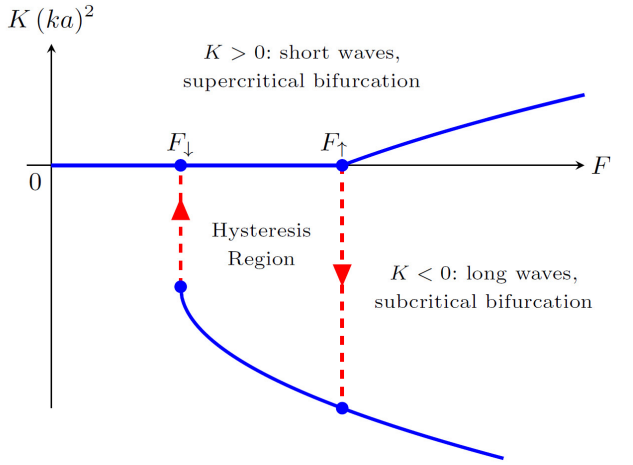


FIG. 2 Theoretical bifurcation diagram (from Rajchenbach & Clamond (2015)). Only the stable branches are displayed in thick blue lines. Rest state is stable only when $F < F_{\uparrow}$. When $K > 0$, only ω_0^- is stable after $F > F_{\uparrow}$; when $K < 0$, only ω_0^+ is stable after $F > F_{\downarrow}$, which makes hysteresis possible.

can be adjusted. A piezoelectric accelerometer GA-YD-107 is mounted on the edge of the platform. The accelerometer transforms the current acceleration to voltage signal which can be displayed and measured on a oscilloscope after the signal is again magnified by a charge amplifier YE5852. Hence, peak-peak voltage V_{pp} of output signal indicates the relative amount of acceleration.

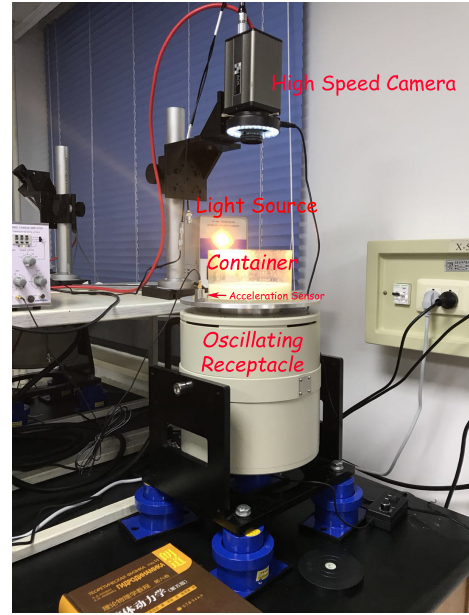


FIG. 3 Experiment setup.

Initially, we used milk, yogurt, Xanthan gum and several combinations of them as fluid samples. To specify, pure milk is used in Section V and a fluid mixture with one portion of 10g/mL Xanthan colloid, one portion of

yogurt and two portions of water is used in Section VI. In every documented experiment, we first fixed frequency and carefully raised amplitude within permissible range. Under every parameter set (Ω, V_{pp}) , the video and measurement of V_{pp} were taken after settle time of approximately 2 min.

IV. ALGORITHMS

A. Non-negative matrix factorization (NMF)

Non-negative matrix factorization (NMF) is based on a general conception: we perceive the world by parts. Rather than a single algorithm, NMF refers to a group of algorithms to factorize a matrix \mathbf{V} into two matrices \mathbf{W} and \mathbf{H} with minimum deviation, which is written in explicit mathematical form as

$$\mathbf{V} \cong \mathbf{WH}, \quad (11)$$

under the requirement of $\min_{W,H} \|V - WH\|_F$, $W \geq 0$ and $H \geq 0$. In practice, we use Lee and Seung's multiplicative update rule (Lee & Seung, 2001) to iterate with a default tolerance of 0.0001. The iterations take steps as followed:

$$H_{[i,j]}^{n+1} = H_{[i,j]}^n \frac{((W^n)^T V)_{[i,j]}}{((W^n)^T W^n H^n)_{[i,j]}} \quad (12)$$

$$W_{[i,j]}^{n+1} = W_{[i,j]}^n \frac{(V(H^{n+1})^T)_{[i,j]}}{(W^n H^{n+1} (H^{n+1})^T)_{[i,j]}} \quad (13)$$

Given a video, i.e. a series of pictures, we first extracted pixel data from each picture to construct the original matrix \mathbf{V} , then we initialize the \mathbf{W} and \mathbf{H} with all elements non-zero. After several iterations by the rules above, we obtained final \mathbf{W} and \mathbf{H} with the minimum deviation. In analogy to partitioned matrix-matrix multiplication, each picture data in the original data could be seen as the product of \mathbf{W} and a part of \mathbf{H} , i.e. a set of fixed pictures and their corresponding coefficients. In this sense, \mathbf{W} can be seen as the eigen-picture matrix with adjustable number of pictures, while \mathbf{H} collects all coefficients needed, thus can be viewed as the coefficient matrix.

Now we attempt to view standing wave in another perspective. Given the fact that adjacent anti-nodes have opposite phases, the holistic scheme could be decomposed into two modes, each representing the areas vibrating under one phase. Then, the entire surface vibration transforms into two modes vibrating with a phase difference of π . Providing the similarity of NMF and standing wave, it is natural to expect when NMF is applied to a Faraday pattern video and the number of eigen-picture is set to be two, the output eigen-pictures will characterize the two opposite modes of standing wave.

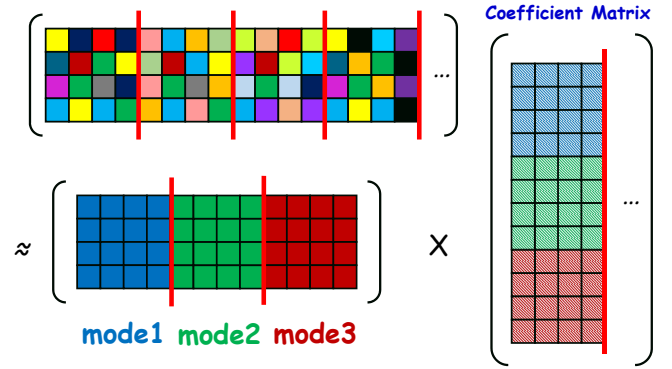


FIG. 4 Illustration for NMF algorithm. Data extracted from original video construct \mathbf{V} . NMF decomposes \mathbf{V} into \mathbf{W} and \mathbf{H} . In analogy to partitioned matrix-matrix multiplication, data of each frame could be seen as the product of \mathbf{W} and a part of \mathbf{H} . In this sense, \mathbf{W} can be seen as the eigen-picture matrix, i.e. modes of oscillation, while \mathbf{H} as the coefficient matrix.

It turns out to be extremely effective, when the input video is processed with NMF, the output pictures shows great regularity and they do not overlap. The region excluded in both pictures represents nodes on standing wave. After we combined two output pictures under different RGB channels (green and blue in this work), a typical situation is shown in Fig. 5.

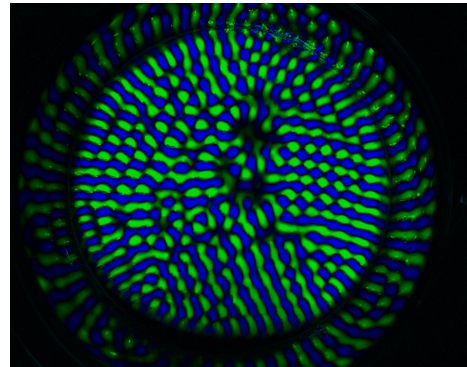


FIG. 5 A typical combination of output pictures. A video of fluid mixture in Section VI driven under 70 Hz is processed with NMF. Green and blue regions show areas oscillating with opposite phases. Dark region indicates nodes on a surface standing wave.

B. Two-point correlation function (2PCF)

In the study of Faraday pattern, the precise measurements of wavelength is necessary. Some authors suggested using two dimensional Fourier transformation (2dFT) which transforms an image from space domain to frequency domain. The energy of low frequency components of the image is distributed near the origin point in

frequency domain, while energy of high frequency component is distributed in the peripheral region. If 2dFT is applied onto a perfect image with smoothly distributed waves, a prominent ring on frequency plane can be found. But in this experiment, wave patterns are sometimes not homogeneous and tend to have locally uniform distribution in relatively small regions, and patterns in different regions are in different modes and along different directions. Thus 2dFT method would be contaminated by low frequency and high frequency noises.

To measure the wavelength with higher precision, we refer to a well-developed method in cosmology and astrophysics to depict the characteristics of fluctuations in the density field, namely the *two-point correlation function* (2PCF). Two-point correlation function has been used in cosmology research, especially in cosmic microwave background (CMB), baryonic acoustic oscillation (BAO), galaxy clusters and dark matter halos (Peebles, 1980). Two-point correlation function denotes the excess probability to find a point over random distribution. If data points are clustered in a given space, two-point correlation function can tell us the inter-cluster spread and inter-cluster separation (Fatemi-Ghomie et al., 1999).

Let δS be an infinitesimal area so that the probability of finding one data point in δS is $O(\delta S)$. Under the first order approximation, the probability of finding a point in area δS is

$$dP = n\delta S, \quad (14)$$

where n is a constant (i.e. number density). Both dP and n depend on the position of δS . The probability of finding a point in δS_1 and another in δS_2 with separation \mathbf{r} is

$$dP_{12} = n^2\delta S_1\delta S_2 [1 + \xi(\mathbf{r}_1; \mathbf{r})]. \quad (15)$$

The existence of $\xi(\mathbf{r}_1; \mathbf{r})$ represents the aggregation behavior of data points in the given plane. If the points are not spatially correlated and distributed randomly, then $\xi(\mathbf{r}_1; \mathbf{r}) = 0$ for all \mathbf{r}_1 and \mathbf{r} . Based on conditional probability $P(A|B) = P(AB)/P(B)$, if we have already found a point in δS_1 , then the probability of finding the corresponding point in δS_2 is

$$d\tilde{P}_{12} = n\delta S_2 [1 + \xi(\mathbf{r}_1; \mathbf{r})]. \quad (16)$$

We can integrate (16) inside an area S_r , which is a circle with center at \mathbf{r}_1 and radius r .

$$N_r(\mathbf{r}_1) = nS_r + n \int_{S_r} \xi(\mathbf{r}_1; \mathbf{r}) dS_2. \quad (17)$$

Note that (17) is the function of the position of first point \mathbf{r}_1 . If we know $\xi(\mathbf{r}_1; \mathbf{r})$, we can repeat the calculation in (17) using different first point \mathbf{r}_1 and these calculations form an ensemble. Taking the ensemble average of all these calculations gives

$$\langle N_r \rangle = nS_r + n \int_{S_r} \langle \xi(\mathbf{r}_1; \mathbf{r}) \rangle dS_2. \quad (18)$$

$\langle N_r \rangle$ means the average number of pairs we can find at distance less than r . The ensemble averaging eliminates the dependence of ξ on \mathbf{r}_1 , and we define this ensemble averaged ξ as two-point correlation function

$$\xi(r) = \langle \xi(\mathbf{r}_1; \mathbf{r}) \rangle. \quad (19)$$

In practice, we can calculate the average number of pairs at distance between r and $r + dr$ from each other, and we define this number as N_p .

$$N_p = \langle N_{r+dr} \rangle - \langle N_r \rangle \quad (20)$$

$$= nL_r dr + n\xi(r)L_r dr, \quad (21)$$

where L_r is the circumference of S_r . Thus we get the two-point correlation function:

$$\xi(r) = \frac{N_p}{nL_r dr} - 1, \quad (22)$$

where dr is the bin size, which can be set arbitrarily in practice.

In this work, two-point correlation function is calculated using the bootstrapped two-point correlation function in python package astroML (Ivezić et al., 2014; Vanderplas et al., 2012). The bootstrapped 2PCF method can also calculate error of correlation function. After NMF decomposition, we choose green channel or blue channel (representing node and antinode) according to the clarity of decomposition. Pixels inside of the circular container whose gray level are higher than 205 are marked as data points. Then we calculated 2PCF of these data points using astroML and obtain $\xi(r)$ as shown in Fig. 6. Equidistant peaks imply that Fig. 5 has good periodic spatial structures. The position of first peak is inter-cluster distance, i.e. wavelength λ in this work. This method provides an effective way to measure pattern wavelength automatically and precisely. But 2PCF doesn't work well for strong stripe pattern and *dipole* pattern. For the latter one, we employ polar transformation.

V. DIPOLE DISPERSION RELATION

Water is considered to be Newtonian fluid, whose kinematic viscosity is relatively small ($\nu = 1.0$ cSt = $1.0 \times 10^{-6} \text{m}^2 \text{s}^{-1}$). For ideal fluid with infinite depth d in boundless container, (2) can be simplified into

$$\omega_0^2 = gk + \frac{T}{g} k^3. \quad (23)$$

One way of checking the validity of NMF algorithm is to measure the dispersion relation of ideal fluid and compare it with (23). Limited by the experiment setup, the reflection on the surface of water will strongly contaminate NMF decompositions. Among fluids with low viscosity ($\nu \sim 10^{-6} \text{m}^2 \text{s}^{-1}$), milk has low surface reflection

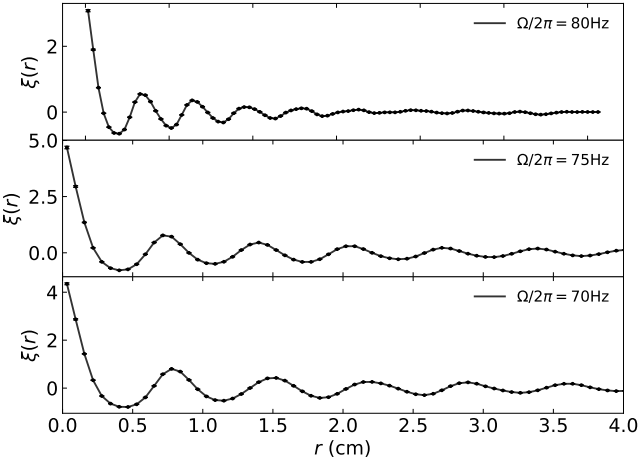


FIG. 6 After NMF decomposition, we choose green channel or blue channel (representing node and antinode) according to the clarity of decomposition. Pixels inside of the circular container whose gray level are higher than 205 are marked as data points. Then we calculated 2PCF ($\xi(r)$) of these data points using astroML and obtain $\xi(r)$ as shown in Fig. 6. Equidistant peaks imply patterns have good periodic spatial structures. The position of first peak is inter-cluster distance, i.e. wavelength λ , in this work.

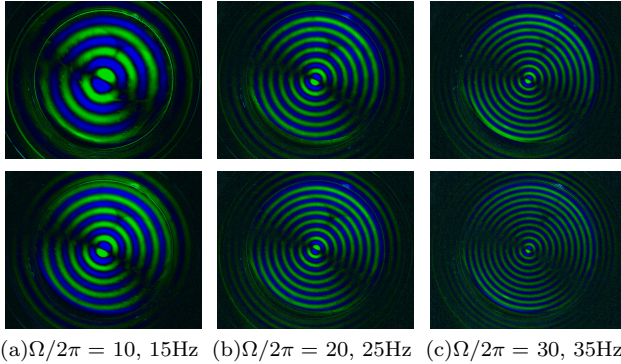


FIG. 7 *Dipole* pattern of milk sample. The driving frequency $\Omega/2\pi$ ranges from 10 Hz to 35 Hz. Wavelengths of *dipole* patterns decreases with the increase of driving frequency Ω . The dispersion relation is shown in Fig. 9.

and high opacity. Hence we use milk to test dispersion relation for ideal fluid with infinite depth, i.e. (23).

In this experiment, the thickness of milk layer is $d = 3$ cm. The upper limit of wavelength in this experiment is the scale of container $l = 13.85$ cm, thus wave vector k of permitted pattern satisfies $k > 2\pi/l \approx 45$. The factor $\tanh kd$ in (2) is in the range of $0.87 < \tanh kd < 1$. Hence (23) is a good approximation under this circumstance.

Examples of the *dipole* patterns of milk sample are shown in Fig. 7. We consider the term *dipole* pattern here to mean that the central region in NMF decomposed image is like a dipole, while the equiphase line are circles

with center on central dipole. Given a driving frequency, *dipole* pattern only appears when the driving force is very low. Hence dipole pattern is in weakly nonlinear region and can be depicted by (23).

To quantify the wavelength of *dipole* pattern, we employ polar transformation method using `polarTransform` (Elliott, 2018) python package. We denote the gray level of a pixel by L . After convert NMF decomposed image from RGB into gray level L , we apply polar transformation $(x, y, L) \rightarrow (r, \theta, L)$ to the gray level image, we get the radial distribution of L for all directions $\theta \in (0, 2\pi)$. We denote gray level profiles as $f(r, \theta)$, where θ is angle parameter. Then stacking $\sum_i f(r, \theta_i)$ was applied to these profiles and it turned out the final gray level profile, see Fig. 8.

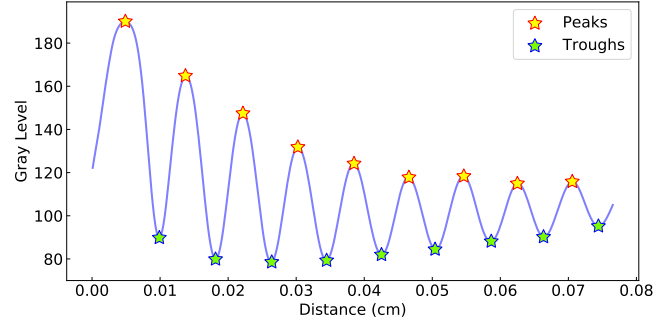


FIG. 8 The gray level profile of *dipole* pattern with driving frequency $\Omega = 20$ Hz. Yellow and green stars represent those detected peaks and troughs, respectively.

The profiles have troughs and peaks. Using peak detecting tool PEAKUTIL (Negri & Vestri, 2017), positions of troughs and peaks can be well determined. At the same time, the mean separation of peaks can be fitted using least square method. Note that mean separation of peaks are derived from the gray scale image, so that the wavelength of *dipole* pattern is two times of this separation. The dispersion relation of *dipole* pattern for milk sample is shown in Fig. 9. We fit the dispersion relation using (23) and obtain $g_{\text{fit}} = 4.44 \text{ kg m s}^{-2}$, $(T/\rho)_{\text{fit}} = 3.82 \times 10^{-5} \text{ m}^3 \text{s}^{-1}$. Red line shows the predicted dispersion line by (23) with $g = 9.8 \text{ kg m s}^{-2}$ and the same T/ρ ratio as the fitted line. From KINO (2014), the surface tension of milk is $T \simeq 40 \text{ mN/m}$ and density of milk is $\rho \simeq 1.035 \times 10^3 \text{ kg m}^{-3}$, thus $T/\rho = 3.90 \times 10^{-5} \text{ m}^3 \text{s}^{-1}$. This result coincide with our fitted parameter quite well. But the fitted gravity g is almost a half of $g = 9.8 \text{ kg m s}^{-2}$. Remember that (23) is valid for boundless container without periodic driving force. Both finite boundary and the driving force here may affect the measurement of g , but driving force has nothing to do with T/ρ .

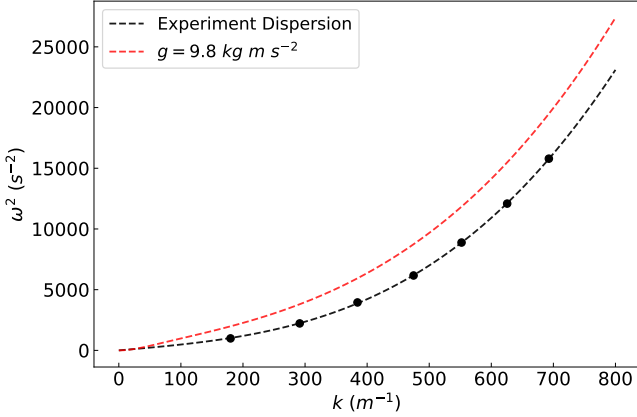


FIG. 9 Dispersion relation of *dipole* pattern for milk sample. Dots are experimental data. We fit the dispersion relation using (23) and obtain $g_{\text{fit}} = 4.44 \text{ kg m s}^{-2}$, $T/\rho = 3.82 \times 10^{-5} \text{ m}^3 \text{s}^{-1}$. Red line shows the predicted dispersion line with $g = 9.8 \text{ kg m s}^{-2}$ and the same T/ρ ratio as the fitted line.

VI. ONSET AMPLITUDE

Aforementioned in Section III, we used a fluid mixture to enhance both non-linearity and opacity, making it more convenient to apply picture processing and data analysis. We modulated frequency from 10Hz to 100Hz under 5 Hz step size. For every fixed frequency, we first finely raised the amplitude until excitation and marked down the corresponding V_{pp} of the accelerometer as $V_{pp\text{-up}}$. Then we raised amplitude up slightly and shoot a video of the fluid surface with high speed camera which was used to calculate wave vector k afterwards. Next we switched down amplitude with care until homogeneous state recovered from excitation. Likewise, the corresponding V_{pp} was recorded as $V_{pp\text{-down}}$.

We found in practice, k is always large enough, partly owing to the finite size of container that only allows relatively short wavelengths. In this case, kd always satisfies $kd \gg 1$ within experimental range. According to (6), when $kd \gg 1$, K barely changes i.e. $K \approx \frac{1}{8} > 0$, thus only ω_0^- branch is stable. Now we can simplify the dispersion relation in (10) into

$$\frac{\omega_0(k)}{\omega} = 1 + \frac{1}{8}(ka)^2 - \sqrt{\frac{F^2}{16} - \frac{\sigma^2(k)}{\omega^2(k)}}. \quad (24)$$

In association with the F_\uparrow expression in (8), we obtained

$$\left(\frac{\omega_0}{\omega} - 1\right) + \left|\frac{\omega_0}{\omega} - 1\right| = \frac{1}{8}(ka)^2. \quad (25)$$

Only if $\omega_0 > \omega$ will the equation make sense, which is further simplified in an alternative expression

$$\omega_0(k) - \omega = \frac{\omega}{16}(ka)^2. \quad (26)$$

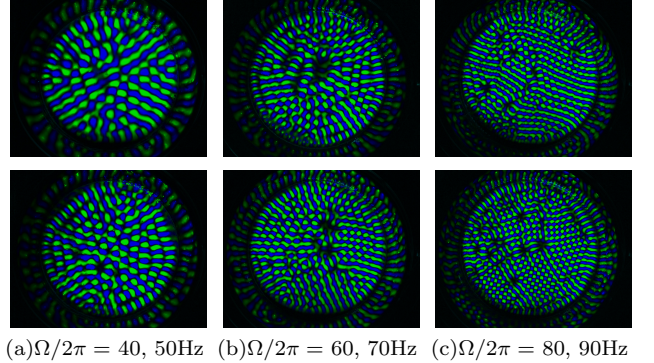


FIG. 10 Faraday patterns near excitation produced by NMF. Driving frequency $\Omega/2\pi$ ranges from 40 Hz to 90 Hz. Wavelengths corresponding to each Ω is calculated with 2PCF.

If there is solution to (26), it will automatically satisfy $\omega_0 > \omega$. Suppose (26) is solvable under appropriate a , we can compare k solved from (26) with k measured in experiments. Moreover, we can also simulate F_\uparrow by plugging in k from (26) into (8). Note that F_\uparrow is the dimensionless forcing given by (2), which gives

$$\Omega^2 \mathcal{A} = F_\uparrow(\omega)(g + \frac{T}{\rho}k^2(\omega)). \quad (27)$$

Assuming $V_{pp\text{-up}}$ has a simple linear relation with acceleration, when we plot both $\Omega^2 \mathcal{A}$ and $V_{pp\text{-up}}$ on logarithmic scale versus linear ω or Ω , they should possess identical shape, barring only a constant vertical deviation.

Some typical examples of pattern near excitation are shown in Fig. 10. The patterns are locally square or hexagonal, demonstrating point-like feature on the whole. Wavelength can be accurately computed by 2PCF under such circumstances. We first fit k versus Ω by (26) under variable parameters except kinematic viscosity ν , since ν does not appear in (26). Then we fit log acceleration versus Ω by only tuning ν to find the most similar shape with an allowable shift. Measured wavevectors and fitted relation by (26) are shown in Fig. 11. Similarly, measured onset amplitude in acceleration form and fitted relation by (27) are shown in Fig. 12.

VII. DISCUSSION

Given the fact that $K > 0$ within experimental range, there should be no hysteresis according to Fig. 2. However, we indeed observed hysteresis, sometimes even quite obvious, in our experiments.

We observed when switching down amplitude, the residual oscillation always appeared on the edge of receptacle, forming a ring-shape pattern. Since all theoretical deduction above is conducted neglecting horizontal boundary, we speculate that the hysteresis we observed

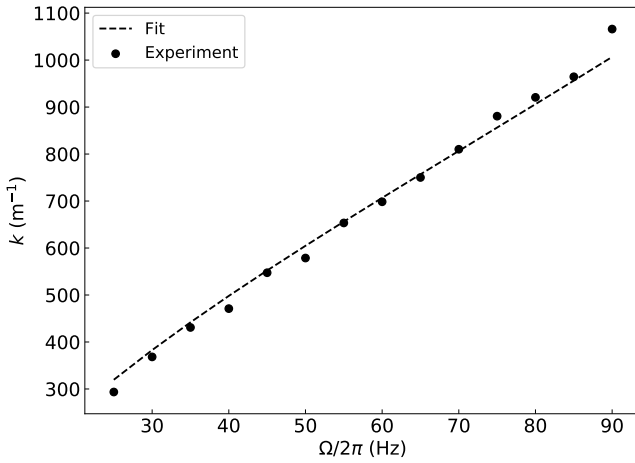


FIG. 11 Dispersion relation of onset region. Black dots represent data points measured in experiments. Black dashed line represents fitted results from (26). Specific parameters are: gravity $g = 9.8 \text{ m/s}^2$, surface tension $T = 2.0 \times 10^{-1} \text{ kg/s}^2$, liquid density $\rho = 2.0 \times 10^3 \text{ kg/m}^3$, depth $d = 3.0 \times 10^{-2} \text{ m}$, constant excitation amplitude $a = 1.7 \times 10^{-3} \text{ m}$.

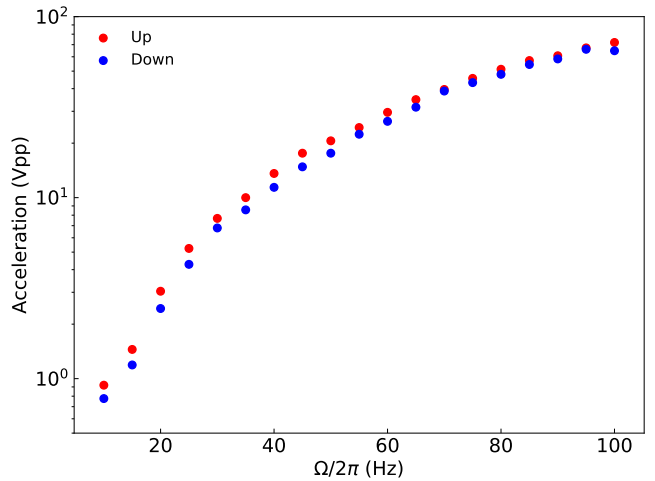


FIG. 13 Hysteresis diagram of fluid mixture. Red dots are the onset acceleration (V_{pp}) when we raised up the amplitude, while blue dots are the onset acceleration (V_{pp}) when we switch down the amplitude.

ACKNOWLEDGMENTS

We thank Wei Wang for experiment setup supporting and her great effort on maintaining the effective operation of laboratory. We thank Luqun Zhou for useful discussions and encouragement. Xiaoyi Ouyang acknowledges Huixia Ren for inspiring the idea of using NMF algorithm on Faraday pattern. Jiaxuan Li acknowledges Dr. Yingjie Peng for introducing 2PCF in his cosmology course. We also thank Wenjun Zhang for many constructive discussions and his monitor.

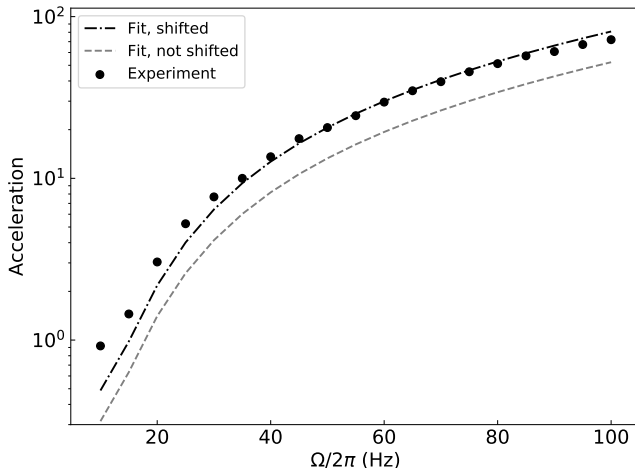


FIG. 12 Log acceleration-frequency relation of onset region. Black dots represent data points measured in experiments. Black dashed line represents fitted results from (27) before shifting. Black dash-dotted line represents fitted results after shifting. Parameters are unchanged except kinematic viscosity μ which is tuned to $\mu = 1.0 \times 10^{-2} \text{ m}^2/\text{s}$.

was a consequence of boundary condition. Further verification requires more experiments with different sizes and shapes of receptacle. Meanwhile, since most excitations originated from the center of receptacle when amplitude was tuned up, we believe $V_{pp,\text{up}}$ is still in consistent with theory, giving the analogous trend shown in Section VI.

REFERENCES

- Abramowitz, M., & Stegun, I. A. 1965, Handbook of mathematical functions with formulas, graphs, and mathematical table, Vol. 2172 (Dover New York)
- Arbell, H., & Fineberg, J. 1998, Physical review letters, 81, 4384
- . 2000, Physical Review Letters, 85, 756
- Benjamin, T. B., & Ursell, F. 1954, Proceedings of the Royal Society of London. Series A, Mathematical and Physical Sciences, 225, 505
- Besson, T., Edwards, W. S., & Tuckerman, L. S. 1996, Physical Review E Statistical Physics Plasmas Fluids & Related Interdisciplinary Topics, 54, 507
- Christiansen, B., Levinsen, M. T., et al. 1992, Physical Review Letters, 68, 2157
- Ciliberto, S., & Gollub, J. 1985, Journal of Fluid Mechanics, 158, 381
- Ding, Y., & Umbanhowar, P. 2005, in Meeting of the Division of Fluid Dynamics, 235–245
- Edwards, W. S., & Fauve, S. 1994, Journal of Fluid Mechanics, 278, 123
- Elliott, A. 2018, polarTransform v1.0.0
- Epstein, T., & Fineberg, J. 2006, Physical Review E, 73, 055302

- Fatemi-Ghom, N., Palmer, P., & Petrou, M. 1999, Journal of Mathematical Imaging and Vision, 10, 7
- Hough, S. S. 1896, Proceedings of the London Mathematical Society, s1-28, 264
- Hunt, J. N. 1964, La Houille Blanche, 685
- Ivezić, Ž., Connolly, A., Vanderplas, J., & Gray, A. 2014, Statistics, Data Mining and Machine Learning in Astronomy (Princeton University Press)
- KINO. 2014, Measured surface tension of common articles of everyday use
- Kudrolli, A., Pier, B., & Gollub, J. P. 1998, Physica D: nonlinear phenomena, 123, 99
- Kumar, K., & Tuckerman, L. S. 1994, Journal of Fluid Mechanics, 279, 49
- Lee, D. D., & Seung, H. S. 2001, in Advances in neural information processing systems, 556–562
- Mermin, N. D., & Troian, S. M. 1985, Physical Review Letters, 54, 1524
- Meron, E. 1987, Physical Review A, 35, 4892
- Milner, S. 1991, Journal of fluid mechanics, 225, 81
- Negri, L. H., & Vestri, C. 2017, lucashn/peakutils: v1.1.0, doi:10.5281/zenodo.887917
- Newell, A. C., & Pomeau, Y. 1999, Journal of Physics A General Physics, 26, L429
- Peebles, P. J. E. 1980, The large-scale structure of the universe (Princeton University Press)
- Porter, J., & Silber, M. 2003, Physica D: Nonlinear Phenomena, 190, 93
- Rajchenbach, J., & Clamond, D. 2015, Journal of Fluid Mechanics, 777
- Skeldon, A. C., & Rucklidge, A. M. 2015, Journal of Fluid Mechanics, 777, 604
- Tadjbakhsh, I., & Keller, J. B. 1960, Journal of Fluid Mechanics, 8, 442
- Vanderplas, J., Connolly, A., Ivezić, Ž., & Gray, A. 2012, in Conference on Intelligent Data Understanding (CIDU), 47–54
- Zhang, W., & Vinals, J. 1997, Journal of Fluid Mechanics, 336, 301